The Three Hundred: Cluster Dynamical States and Relaxation Time Scale

Monthly Notices of the ROYAL ASTRONOMICAL SOCIETY

MNRAS **516,** 26–38 (2022) https://doi.org/10.1093/mnras/stac2171
Advance Access publication 2022 August 1

THE THREE HUNDRED: cluster dynamical states and relaxation period

Bowei Zhang,[1,2]★ Weiguang Cui ,[1,3]★ Yuhuan Wang,[1] Romeel Dave [1] and Marco De Petris[4]

[1]*Institute for Astronomy, University of Edinburgh, Royal Observatory, Edinburgh EH9 3HJ, UK*
[2]*Department of Applied Mathematics and Theoretical Physics, University of Cambridge, Cambridge CB3 0WA, UK*
[3]*Departamento de Física Teórica and CIAFF, Modulo 8, Universidad Autónoma de Madrid, E-28049 Madrid, Spain*
[4]*Dipartimento di Fisica, Sapienza Universitá di Roma, Piazzale Aldo Moro, I-5-00185 Roma, Italy*

Accepted 2022 July 26. Received 2022 July 26; in original form 2021 December 6

ABSTRACT

We introduce a new parameter λ_{DS} to quantify the dynamical state of galaxy clusters and test it using simulations from THE THREE HUNDRED cluster zoom suite. λ_{DS} is a combination of three previously used dynamical state measures, namely virial ratio, centre of mass offset, and substructure mass fraction, crafted to assume a double-Gaussian distribution, thereby yielding a natural division between relaxed and unrelaxed clusters where the Gaussians cross. Using dark matter-only simulations, we identify the optimal separator to be $\lambda_{DS} = 3.424$. We test this same criterion on two sets of fully hydrodynamical THE THREE HUNDRED runs (GADGET-X and GIZMO-SIMBA), and find only a weak dependence on the input baryonic physics. We correlate the evolution of λ_{DS} with the mass accretion history and find that halo mass changes of $\frac{\Delta M_{200}}{M_{200}} \lesssim 0.12$ do not typically alter the dynamical state. We examine the relaxation period, defined as the time taken to return to relaxation after becoming disturbed, and find a correlation between this relaxation period and the strength of halo mass change $\frac{\Delta M_{200}}{M_{200}}$. By fitting this correlation, we show that the relaxation period can be estimated from $\frac{\Delta M_{200}}{M_{200}}$ (even for multiple mass accretion events) with good accuracy.

Key words: galaxies: clusters: general – galaxies: evolution – galaxies: haloes.

1 INTRODUCTION

Galaxy clusters are the largest gravitationally bound structures in the Universe, and as such they are highly studied objects both observationally and theoretically. In the current cosmological paradigm, clusters grow via hierarchical structure formation from the assembly of smaller structures, and since they are the largest virialized objects, they are still in the process of assembling today. Thus it is interesting to examine and quantify the dynamical state of clusters, i.e. how close to virial relaxation it is at any given time, since this is an important consideration when trying to e.g. estimate cluster masses from observations for constraining cosmological parameters (e.g. Nelson et al. 2012; Biffi et al. 2016; Gianfagna et al. 2021), measure cluster formation times (e.g. Mostoghiu et al. 2019), and constrain cluster concentrations (e.g. Neto et al. 2007).

Hierarchical merging can temporarily displace clusters from virial equilibrium, and thus provide unique events to study a range of physical processes (e.g. Poole et al. 2006a; Zenteno et al. 2020). Disturbed clusters provide test bed for ΛCDM model (e.g. Thompson, Davé & Nagamine 2015; Kim, Peter & Wittman 2017; Sereno et al. 2018), and their enhanced strong lensing efficiency provides powerful tools to investigate the universe at high redshift (see Baldi et al. 2013; Acebron et al. 2019, for example). The cluster dynamical state also impacts the properties of galaxies within clusters. For example, Morell et al. (2020) found that galaxies evolve in the same way into a Gaussian or non-Gaussian velocity distribution system (classified as relaxed or unrelaxed clusters), but their formation histories lead to different mixtures of galactic types and infall patterns. Furthermore, disturbed clusters can be used to examine the most extreme ram pressure events and study the cluster intracluster medium (ICM) thanks to so-called jellyfish galaxies (McPartland et al. 2015). Lastly, it has been found that the halo formation time affects the central BCG properties (Cui et al. 2022, see also Cui et al. 2021 for a similar result at lower halo masses), thus this can be also linked to the cluster dynamical state.

The recent formation history of galaxy clusters correlates strongly with its degree of dynamical equilibrium (e.g. Wong & Taylor 2012), since an active recent merger history is more likely to result in a cluster departing from virialization. As a result, galaxy clusters can have a wide range dynamical states, which, at a basic level, can be roughly classified into two categories: relaxed (or virialized) and non-relaxed (or non-virialized). Relaxed clusters are expected to have a nearly spherical shape and a Gaussian line-of-sight velocity distribution (e.g. Faltenbacher & Diemand 2006), while non-relaxed clusters can show elongated shapes (Gouin, Bonnaire & Aghanim 2021), non-Gaussian velocity distributions (Hou et al. 2009), the presence of massive substructures (Lopes et al. 2018), and irregular morphological properties (e.g. Mantz et al. 2015; De Luca et al. 2021). Quantifying how these (potentially) observable properties correlate with the cluster's dynamical state is thus of significant interest for using clusters as a testbed for cosmology and galaxy evolution.

To this end, many different approaches for classifying cluster dynamical states and assessing the relaxation degree of clusters have been developed, both theoretically using simulations (see Cui et al.

★ E-mail: bz287@cam.ac.uk (BZ); cuiweiguang@gmail.com (WC)

2017, and references therein), and in observations (see De Luca et al. 2021, and references therein). In observations, cluster dynamical states can be classified by examining both the galaxy population and the X-ray emitting ICM. Wen & Han (2013) developed methods to quantify the substructure and dynamical state of galaxy clusters by using photometric data from the Sloan Digital Sky Survey. Capalbo et al. (2021) and De Luca et al. (2021) investigated the correlation between cluster dynamical states and cluster morphology measured through images of the surface brightness in the X-ray band and using the thermal Sunyaev-Zel'dovich effect. In simulations, there are a variety of ways the halo dynamical state can be evaluated. Using dark matter-only (DMO) simulations, Bett et al. (2007) used the integrated virial ratio $2T/|W| + 1$ to classify dynamical states, and suggested $2T/|W| + 1 < 1.5$ to select haloes in quasi-equilibrium states. Neto et al. (2007) expanded the criteria by including substructure mass fraction and centre-of-mass offset, which contain the information of the constituents in the cluster and the shape of cluster, respectively. Shaw et al. (2006) additionally took the surface pressure energy E_s into account in virial ratio calculation (see also Cui et al. 2017, for detailed calculation for hydrodynamic simulations). Davis, D'Aloisio & Natarajan (2011) found the effect of the potential energy from particles outside of haloes is negligible.

A drawback of all these methods, both observational and theoretical, is that they usually yield a unimodal distribution for their dynamical state parameter (in either single or combined parameters; Haggar et al. 2020; De Luca et al. 2021). As a result, the threshold for demarcating relaxed versus unrelaxed clusters (in order to e.g. select a sample of relaxed clusters) is not obvious, and is often chosen somewhat arbitrarily. It would be more satisfying if a dynamical state parameter could be constructed that displayed a more bimodal distribution, for which the separation between relaxed and unrelaxed objects could be more robustly determined. Importantly, this parameter must be relatively insensitive to the detailed baryonic physics, since the complex interplay particularly of feedback processes within a cluster is currently not well-understood. Developing a dynamical state measure satisfying these constraints will be our first key goal in this paper.

Such a quantity is useful towards more rigorously studying how the cluster dynamical state evolves. For instance, one key question that is not so thoroughly studied in the literature is the relaxation time-scale of the cluster dynamical state, i.e. how long does it need from being disturbed to relaxing back into hydrostatic equilibrium, which could help us understand cluster thermalization (Sereno et al. 2021). In this work, as an application of our newly developed dynamical state, we quantify the relaxation time-scale of clusters.

To conduct these investigations, we will utilize the large and mass-complete sample of cluster zoom re-simulations from THE THREE HUNDRED project. This suite contains 324 cluster simulations run in DMO mode, and also with two modern galaxy evolution models, including active galactic nucleus (AGN) feedback. Furthermore, it evolves large zoom regions out to at least $5\times$ the virial radius, meaning that the dynamics of infalling objects can be tracked reliably. The large and homogeneous sample is critical for developing and exploring our dynamical state measure.

The layout of this paper is as follows: we introduce the THE THREE HUNDRED project in Section 2. The new parameter-free cluster dynamical classification method and separation of relaxed and unrelaxed clusters are presented in Section 3. Our main results on the cluster dynamical state are shown in Section 4. We finally conclude and discuss our study on cluster dynamical state in Section 5.

2 THE THREE HUNDRED PROJECT

The THE THREE HUNDRED[1] consists of 324 resimulated clusters and 4 field regions extracted from the MultiDark Planck simulation, MDPL2 (Klypin et al. 2016). The MDPL2 simulation has cosmological parameters of $\Omega_M = 0.307$, $\Omega_B = 0.048$, $\Omega_\Lambda = 0.693$, $h = 0.678$, and $\sigma_8 = 0.823$. All the clusters and fields have been simulated using the full-physics hydrodynamic codes GADGET-X (GX in short, Rasia et al. 2015; Steinborn et al. 2015; Beck et al. 2016), GADGET-MUSIC (Sembolini et al. 2013), and a version of GIZMO-SIMBA (Davé et al. 2019) re-tuned slightly to the lower resolution of THE THREE HUNDRED (Cui et al. 2022). The first two are based on GADGET2 (Springel 2005) using smoothed particle hydrodynamics, while the latter is based on the GIZMO code (Hopkins 2015) using Meshless Finite Mass hydrodynamics. In the resimulation region, the mass of dark matter and gas particles are $12.7 \times 10^8\, h^{-1}\mathrm{M}_\odot$ and $2.36 \times 10^8\, h^{-1}\mathrm{M}_\odot$, respectively. Each cluster resimulation consists of a spherical region of radius $15\, h^{-1}$Mpc at $z = 0$ centred on one of the 324 largest objects within the host MDPL2 simulation box, which is $1\, h^{-1}$ Gpc on a side. The halo masses of central galaxy clusters range from $6.4 \times 10^{14}\, h^{-1}\mathrm{M}_\odot$ to $2.63 \times 10^{15}\, h^{-1}\mathrm{M}_\odot$.

A more detailed introduction of THE THREE HUNDRED can be found in Cui et al. (2018). Besides these studies on the cluster dynamical state which has been mentioned in the introduction, these simulated galaxy clusters have been used for different proposes: the filaments around the clusters (Kuchner et al. 2020, 2021; Kotecha et al. 2022; Rost et al. 2021); the backsplash galaxies (Haggar et al. 2020; Knebe et al. 2020), and shock radius (Baxter et al. 2021; Anbajagane et al. 2022b). The advanced baryon models in hydrodynamic simulations allow us to perform a detailed investigation on the cluster properties, such as profiles (Mostoghiu et al. 2019; Li et al. 2020), substructure and its baryonic content (Arthur et al. 2019; Haggar et al. 2021; Mostoghiu et al. 2021b, a), the cluster (non-)thermalization (Sayers et al. 2021; Sereno et al. 2021), the fundamental plane (Díaz-García et al. 2022), and the cluster mass bias (Ansarifard et al. 2020; Li et al. 2021; Anbajagane et al. 2022a). Additional runs allow us to investigate more things: such as the effect of environment by comparing to void/field regions (Wang et al. 2018); constraining the dark matter cross-section with the self-interacting dark-matter run (Vega-Ferrero et al. 2021); examining the chameleon gravity (Tamosiunas et al. 2022).

In this paper, we only use the haloes identified by the Amiga's Halo Finder (AHF; Knollmann & Knebe 2009) with a spherical overdensity of $200\rho_{crit}$. The progenitors of these haloes are tracked and identified using the MERGERTREE that is part of the AHF package. We only focus on the main progenitors of the cluster, which is defined as the highest matched halo in the previous snapshot, for tracking their mass accretion history.

3 CLASSIFYING CLUSTER DYNAMICAL STATES

This paper aims to determine a new statistic for the dynamical state of clusters that provides a cleaner separation between relaxed and unrelaxed systems. In this section, we review various dynamical state parameters employed in the literature, including a combination of parameters introduced by Haggar et al. (2020) on which we base our statistic, and then develop our optimized combined statistic designed to best satisfy our goals.

[1] https://the300-project.org

3.1 Dynamical parameters and previous work on classifying cluster dynamical states

In the literature (see e.g. Cui et al. 2017), various parameters have been used to describe the dynamical states of clusters. Among the most commonly used parameters are:

(i) The virial ratio, η.

The exact expression for the virial theorem is

$$\frac{1}{2}\frac{\mathrm{d}^2 I}{\mathrm{d}t^2} = 2T + W - E_s \tag{1}$$

where I is the moment of inertia, T and W are kinetic energy and potential energy respectively, and E_s is the energy from surface pressure P.

If the cluster system is in dynamical equilibrium, equation (1) will reduce to

$$2T + W - E_s = 0, \tag{2}$$

which can be rewritten as

$$\frac{2T - E_s}{|W|} = 1. \tag{3}$$

Therefore, the virial ratio is defined as

$$\eta = \frac{2T - E_s}{|W|}, \tag{4}$$

and a relaxed cluster is expected to have $\eta \approx 1$.

In principle, any system with $\eta \neq 1$ is out of equilibrium. But typically, clusters with η close to 1 are still considered to be in equilibrium. Since this statistic typically shows a unimodal distribution for simulated clusters, there is no obvious boundary on how far away from $\eta = 1$ a cluster is required to be in order to be considered unrelaxed or out of dynamical equilibrium. In our case, we adopt the quantity $|\eta - 1|$ as a measure for the how far out of equilibrium a system is, which we will incorporate in our measure.

(ii) Subhalo mass fraction, f_s.

f_s represents the fraction of the mass of the cluster contained in subhalos, in our case as identified by AHF. However, this fraction does not include the most massive central substructure since it includes all the particles that do not bound to any other substructures.

For the most relaxed clusters, the subhalo mass fraction should be fairly small, $f_s \lesssim 0.1$. However, in the case where a large subhalo that has recently fallen in and not yet dynamically relaxed, there will be substantial mass within this subhalo. Hence f_s effectively serves as a measure of how far out of equilibrium a cluster is.

(iii) Centre of Mass Offset, Δ_r.

The offset of the centre of mass of cluster is defined as

$$\Delta_r = \frac{\mathbf{R}_{cm} - \mathbf{R}_c}{R_{vir}}, \tag{5}$$

where R_{vir} is virial radius, within which virial theorem applies for a bound system, $\mathbf{R}_c$ is the cluster centre, here the density peak of the cluster from AHF, and $\mathbf{R}_{cm}$ is the position of the centre of mass.

A gravitationally bounded system in equilibrium should have a symmetric mass distribution, which would give a vanishing distance between the centre of mass and the peak of density. In the case of a cluster merger, however, the density peak will typically be at the location of the largest galaxy, while the centre of mass will be somewhere between the main halo and the merging object, leading to a non-zero value for Δ_r. Therefore, Δ_r provides another measure for how far a cluster is out of dynamical equilibrium.

We emphasize here that all the three parameters are only phenomenological descriptions[2] of the cluster dynamical state due to the lack of a physically defined quantity for it. Furthermore, it is not clear which parameter contributes more to or describes better the cluster dynamical state. Therefore, varying criteria are applied to classify a cluster as relaxed. For example, Cui et al. (2017) concluded that a relaxed cluster should satisfy three criteria: $\Delta_r < 0.04, f_s < 0.1$, and $0.85 < \eta < 1.15$. With these criteria, Haggar et al. (2020) combined these three parameters that are normalized to their thresholds but with equal weight, to a continuous, non-binary measure of cluster dynamical states, which is defined as the 'relaxation' parameter of the cluster, χ_{DS}:

$$\chi_{DS} = \sqrt{\frac{3}{\left(\frac{f_s}{0.1}\right)^2 + \left(\frac{|1-\eta|}{0.15}\right)^2 + \left(\frac{\Delta_r}{0.04}\right)^2}} \tag{6}$$

For a cluster to be dynamically relaxed, it requires Δ_r and f_s to be minimized, and $\eta \approx 1$. Therefore, the most relaxed clusters are expected to have large χ_{DS} ($\chi_{DS} > 1$). This is the criterion forwarded by Haggar et al. (2020).

However, there is no distinct separation between the relaxed and unrelaxed clusters; the distribution of the χ_{DS} exhibits a curve closer to single peak Gaussian (see fig. 2 of Haggar et al. 2020). Thus, while $\chi_{DS} = 1$ is a reasonable choice to classify a cluster's dynamical state into relaxed and unrelaxed, it remains unsatisfyingly arbitrary.

3.2 The threshold-free λ_{DS} function

As discussed before, the common issue in all previous works of classifying cluster dynamical states with either single or multiple dynamical parameters is that the thresholds for these parameters are chosen arbitrarily. In order to overcome such issue, we assume that a mass-complete cluster sample at $z = 0$ can be roughly separated into dynamically relaxed and unrelaxed from the DMO simulations. Note that the mass-complete sample is required as the λ_{DS} will be biased to the sample if it is selected in particular ways.

Here, we introduce a new relaxation parameter, λ_{DS}, which is a generalized version of equation (6) from Haggar et al. (2020):

$$\lambda_{DS} = \sqrt{\frac{3}{(a \times \Delta_r)^2 + (b \times f_s)^2 + |1-\eta|^2}}. \tag{7}$$

Instead of using specific pre-factors of Δ_r and f_s terms, we allow these pre-factors a and b to be varied in such a way that λ_{DS} has as close to a double-Gaussian distribution as possible. Since we only care about the distribution of λ_{DS} and not about its absolute values, the critical aspect in equation (7) is the relative contributions from the three denominator terms. Therefore, we can arbitrarily set one term's prefactor in the denominator to be unity with no loss of generality, which we choose to do for the $|1\text{-}\eta|$ term.

To determine the optimal values for a and b, we use the DMO simulation sample from THE THREE HUNDRED. Using the DMO runs allows us to define the values based on a robust and reproducible methodology, which shows little variations among different codes (e.g. Sembolini et al. 2016a, b), even if it does not yield realistic clusters which can be significantly affected by baryonic physics (e.g. Cui et al. 2016; Elahi et al. 2016).

[2] η is the closest one to the physical definition of dynamical equilibrium with $\eta = 1$. However, the cluster can not be treated as an isolated object. For example, even with the surface pressure correction term, we cannot fully correct η for the effects of the potential coming from a nearby object.

In order to classify the clusters into two families, we choose a functional form for the distribution of λ_{DS} as a double Gaussian. The pre-factors a and b can then be determined by fitting the distributions of λ_{DS} with a double-Gaussian function, and finding out the pair of a and b which can give the 'best' double Gaussian distribution, which we describe next. After the two families of clusters are fitted, it is natural to use the crossing point of the two Gaussian curves as the threshold for separating the cluster into relaxed and unrelaxed.

3.3 Determine coefficients *a* and *b*

To determine the a and b parameters, we first compute λ_{DS} for each cluster in the DMO THE THREE HUNDRED runs at redshift 0, for parameters (a, b), both ranging from 0 to 15, in steps of 0.01. For each parameter pair, we fit a double-Gaussian function with the free parameters c_1, c_2, μ_1, μ_2 and σ_1, σ_2 to be determined by

$$f(x) = c_1 e^{-\frac{(x-\mu_1)^2}{2\sigma_1^2}} + c_2 e^{-\frac{(x-\mu_2)^2}{2\sigma_2^2}}. \quad (8)$$

Several criteria are made to select the best a and b values:

(i) the list of λ_{DS} must *not* pass the Shapiro–Wilk test (Shapiro & Wilk 1965), which tests whether a normal distribution can be fit with a single peak. *shapiro*() function can be directly imported from *scipy.stats*, and it will return an indicator called P_{value} when acting on a list-like object. The distribution is normal if its P_{value} is greater than 0.05. For our selected range of a and b with a range which yield the results that fit most with 2500 pair of data. 0.05 is chosen for the threshold to reject the Gaussian distribution, as when it is below 0.05, a smaller number does not necessarily provide a better double Gaussian fit.

(ii) Six parameters (c_1, c_2, μ_1, μ_2, σ_1, and σ_2) are obtained from fitting the double-Gaussian distribution. In a well-behaved double-Gaussian function, the two peaks are expected to have similar heights, similar widths, and be relatively well-separated. Therefore, additional exclusionary criteria are set to be $|c_1 - c_2| > 10$ (heights too different), $|\mu_1 - \mu_2| < 0.2$ (small separation, in log scale), and $|\sigma_1 - \sigma_2| > 0.05$ (widths too different).

After excluding all (a, b) pairs with the above criteria, we select the best set of values to be the one which has the smallest fitting error E, given by the quadrature sum of the difference between the true λ_{DS} distribution and the fitting function.

The best-fitting parameters for the DMO run are $a = 7.30$ and $b = 0.30$. We note that the equivalent values from Haggar et al. (2020) would be $a = 3.75$, $b = 1.5$, with the pre-factor for the $|1 - \eta|$ term scaled out. Hence our double Gaussian criterion preferentially weights the Δ_r (centre-of-mass offset) term more and the f_s (substructure mass) term less compared to the $|1 - \eta|$ term. For the best-fitting distribution, the values for c_1, c_2, μ_1, μ_2, σ_1, σ_2, and E are 35.35, 30.38, 0.34, 0.80, 0.18, 0.13, and 115.20, respectively.

The λ_{DS} distribution with the fitting results is plotted in Fig. 1. The underlying distribution of λ_{DS} for our chosen (a, b) is shown as the blue histogram. The red line shows the best-fitting double Gaussian, and the orange and green lines are the individual Gaussians.

It is evident that the double Gaussian provides a good fit to the distribution. The distribution itself is not obviously bimodal, but none the less is statistically poorly fit by a single Gaussian (Shapiro–Wilk $p = 0.01$). The two underlying Gaussians are well-separated, and of similar height and width, which satisfy our criteria for selecting (a, b).

The double-Gaussian distribution of λ_{DS} avoids the arbitrary choice of the threshold for separating dynamically relaxed and unrelaxed clusters modulo that the assumption of the Double-Gaussian distribution with similar height and width restricts the shape of the λ_{DS} distribution. The threshold for λ_{DS} is naturally defined as the x coordinate of the crossing point of two Single-Gaussian functions, see Fig. 1. For our best-fitting distribution, the threshold value is $\lambda_{DS} = 3.424$.

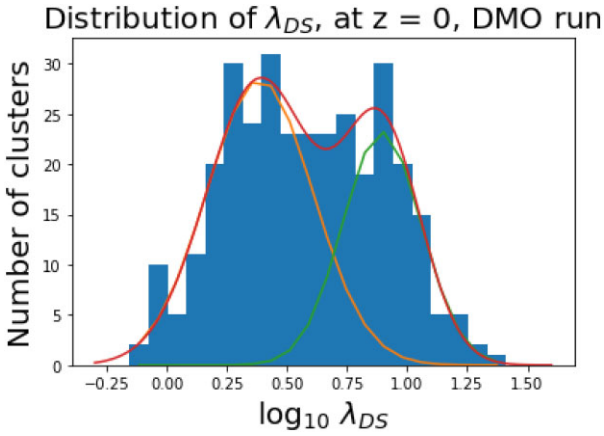

Figure 1. Distributions of the relaxation parameter, $\log_{10}\lambda_{DS}$, for the mass-complete cluster sample from the DMO run, at redshift $z = 0$. The best-fitting parameters are $a = 7.30$ and $b = 0.30$. Red line represents the fitted Double-Gaussian distribution. The two single-Gaussian functions are represented by orange and green line.

We note that the fitting parameters, a and b, and thus the threshold for separating relaxed and unrelaxed clusters, can be sample dependent; reducing or increasing the minimum cluster mass in the mass-complete sample can change a and b slightly. However, we are limited to our sample in this study, and as long as we are consistent, our results will not quantitatively change. This is because these three key quantities: f_s, Δ and η are unit-less, which do not depend on mass or redshift. Therefore, the same λ_{DS} classified as relaxed at $z = 0$ or for cluster with higher mass, should be equally relaxed at high z or a lower mass. Further investigation regarding the changes of a and b with different samples requires a much larger simulation suite, we leave it for a later study.

3.4 The relationship between λ_{DS} and χ_{DS}

Our new dynamical relaxation parameter, λ_{DS}, is based heavily on χ_{DS} (equation 6; Haggar et al. 2020). Earlier, we showed that the optimized parameters λ_{DS} provide a different weighting for the various terms as compared to χ_{DS}. Here, we explore the differences in these two measures in more detail, and compare them head to head.

Fig. 2 shows a comparison of the values of λ_{DS} versus χ_{DS} for the DMO sample of THE THREE HUNDRED clusters. The correlation between λ_{DS} and χ_{DS} is almost linear, showing that both methods classify clusters into relaxed and unrelaxed systems broadly similarly.

Haggar et al. (2020) split the sample into relaxed clusters ($\chi_{DS} > 1.030$), unrelaxed clusters ($\chi_{DS} < 0.619$), and intermediate with $0.619 < \chi_{DS} < 1.030$. The two thresholds from Haggar et al. (2020) are represented by two red vertical lines in. In our work, a single threshold, $\lambda_{DS} = 3.424$, is determined from a systematical way, which is represented by the green horizontal line.

Most clusters classified as relaxed or unrelaxed by Haggar et al. (2020) have a similar classification with our parameter. This means,

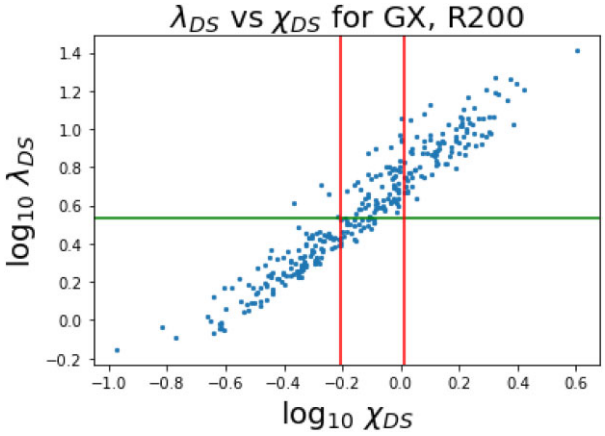

Figure 2. λ_{DS} versus χ_{DS} in logarithm scale for 324 clusters, at z $= 0$, in GX run, which Haggar et al. (2020) used. Two red vertical lines represent the threshold on χ_{DS} for relaxed clusters and unrelaxed clusters, which are $\chi_{DS} =$ 1.030 and $\chi_{DS} = 0.619$, respectively. The green vertical line represents the threshold on λ_{DS}, which is $\lambda_{DS} = 3.424$.

although our new relaxation parameter λ_{DS} adjusts the relative contributions between dynamical parameters η, f_s and Δ_r to rescale and redistribute the old relaxation parameter χ_{DS}, it is still monotonically correlated and does not qualitatively change the results from previous works on classifying cluster dynamical states. None the less, the non-arbitrary classification procedure to obtain λ_{DS} makes classifying dynamical states more robust, reproducible, and extensible to other mass and redshift ranges.

We do not directly connect λ_{DS} with observation classification methods, such as morphology (see De Luca et al. 2021, for example), velocity distribution deviation (see Roberts & Parker 2017; de Carvalho et al. 2017, for example) or the projected phase space of cluster galaxies (Pasquali et al. 2019). However, we note that the connection between χ_{DS} and observational methods has been studied in De Luca et al. (2021), which has shown a good correlation between them. Given the broad similarity of λ_{DS} in terms of classification, we expect that this will provide a similarly good correlation with observational approaches.

4 APPLICATIONS

4.1 The effect of baryons

Different hydrodynamical simulations use different baryonic models, which can result in different best-fitting Double-Gaussian functions. For simplicity in this investigation, and to highlight the changes due to different baryon models, we apply the same fitting results from DMO fitting as the baseline, i.e. with $a = 7.3$, $b = 0.3$, to calculate λ_{DS} in GX and GIZMO runs. See Section A for more information. Nevertheless, by applying the same parameters with threshold, we can examine the effects of baryons. For example, with the same threshold, $\lambda_{DS} = 3.424$, applied to GX and GIZMO run, we find that 151/171/170 clusters are classified as relaxed clusters in DMO/GX/GIZMO run. It looks that hydrosimulations with baryon model tend to increase the number of relaxed clusters. More details will be presented in Section 4.1.

We further investigate the baryon effect on dynamical parameters η, f_s, Δ_r, and λ_{DS}. We matched the corresponding clusters from different runs at $z = 0$. For each cluster, the differences in these parameters between hydrodynamical simulation (GX or GIZMO) and DMO simulation are shown in Fig. 3. Distributions of these differences are plotted in histograms. Then, for each parameter, the median numbers of these differences are used to quantify the baryon effect. Those median numbers and standard errors are marked as vertical lines in Fig. 3 and listed in Table 1. The main results of baryon effects are discussed below:

(i) η from the GX run and the GIZMO run are reduced by about 2 per cent compared to the median value from the DMO run. The differences distribution between the two hydrodynamical simulations is very small, which gives the insight that the impact on η depends weakly on baryon models. Cui et al. (2017) showed a similar result on the weakly model-dependent effect of the decrease in η, but with a more significant difference, about 10 per cent, for cooling, star forming and feedback (CSF) run and AGN run. Here, CSF run refers to a hydrodynamical simulation ignoring the AGN feedback, and the AGN run includes AGN feedback. They also concluded that the ratio between η from the hydrodynamical run and η from DMO run shows no dependence on cluster mass.

(ii) Standard deviations of the differences between Δ_r from GX/GIZMO run and from DMO the run are comparable to the scale of the median number of Δ_r from the DMO run, which shows the scattering distribution of Δ_r in hydrodynamical simulation, in agreement with the result in Cui et al. (2017). This is because the position of the substructure can be largely affected by baryons. However, the average amount of change for all clusters is small, which behaves as a slight decrease about 5 per cent compared to the DMO run. This could be mainly caused by the central galaxy formation, which deeps the potential and increases the halo concentration. Thus, more weights are contributed from the central region.

(iii) Compared to the DMO value, f_s increases by 17 per cent in the GIZMO run. This is in agreement with the result on Cui et al. (2017): their CSF run increases the f_s by 40 per cent for higher cluster mass and by 20 per cent for clusters with lower abundances.
However, the median change of f_s in GX run is negligible, smaller than 5 per cent. The difference between f_s from GX run and GIZMO run should come from the feedback models that control the galaxy formation in these less-massive substructures. The comparison of satellite stellar mass function in Cui et al. (2022) makes it clear that the satellite stellar-mass function from the GIZMO run agrees better with the observation results at lower galaxy mass than GX, which is about five times lower.

(iv) λ_{DS} in GX (GIZMO) run is 9 (6) per cent higher than in DMO run, which indicates a weak baryon-model dependence of λ_{DS}. This is not surprising as the baryon models weakly influence the individual parameters.

4.2 Dynamical state and cluster mass accretion history

It is clear that the cluster dynamical state changes are caused by the accretion of mass, especially in the case of major merger events (see Poole et al. 2006b; Sampaio et al. 2021, for example). However, it is unclear how significant the cluster dynamical state can be altered and how long the cluster will return to a relaxed state after a merger event. In this section, we will try to quantify the relationship between cluster dynamical states and the mass changes and investigate the relaxation time scale – from the beginning of a disturbance to the final relaxed state (see more details in the following section). In Fig. 4, we illustrate the evolution tracks of λ_{DS} and $\frac{\Delta M_{200}}{M_{200}}$ over time for one arbitrary example cluster, where the variation $\Delta M_{200}$is estimated by M_{200} in the snapshot i minus M_{200} in snapshot i-1. The original

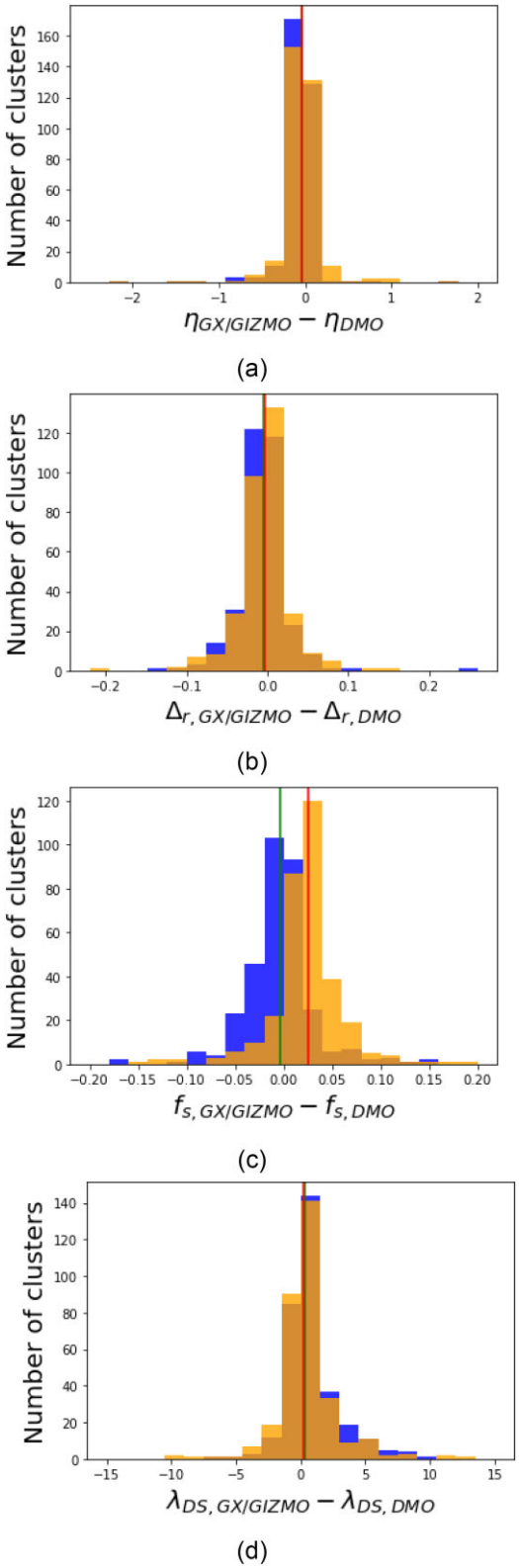

Figure 3. Distributions of the relative differences for (from top to bottom) η, $\Delta_r, f_s, \lambda_{DS}$ between GX (blue histograms) or GIZMO (orange histograms) run and DMO run. Green (red) vertical lines represent the median number of differences for GX (GIZMO) run.

behaviour of the evolution track of λ_{DS} is highly jagged because of the frequent mergers along with difficulties in correctly tracking the progenitors in the simulation, so the function $savagol\_filter$ from *SciPy.signal* is applied to smooth the evolution curve (see scipy.org). In this function, the length of the filter window is set to be 11 data points, and the order of the polynomial to fit the sample is set to be 3. Note that relaxation time-scale estimated in this way is depending on λ_{DS}. Furthermore, this estimation differs from the standard relaxation time-scale calculation based on two-body relaxation (Binney & Tremaine 1987). This is because the latter is only true when the system is isolated, while our calculation is more practical considering the merger events during the cluster's evolution. Therefore, we use the relaxation period for our calculation to distinguish them later.

4.3 The cluster relaxation period

To investigate the evolution of cluster dynamical states, we define the 'relaxation period' to describe the time taken by a cluster to evolve from a relaxed state to an unrelaxed state and then return to the relaxed states. As shown in Fig. 5, one relaxation period starts with the local maximum of λ_{DS} above the threshold before decreasing, after which the λ_{DS} of cluster continues decreasing until it reach some local minimum below the threshold. Then, the relaxation period ends with the first crossing point between λ_{DS} evolutionary track and the threshold, through which the cluster return to a relaxed state again. Note that we exclude the evolution track in the very beginning 4 Gyrs. This is because the halo still have a small mass, and its dynamical state can be dramatically changed due to frequent merging events. Our definition of this relaxation period is very similar to the merger time, which is defined in Contreras-Santos et al. (2022). We share the same initial point to mark the start of relaxation period. However, Contreras-Santos et al. (2022) requires the cluster returning to a following peak of the dynamical relaxation parameter for the end, instead of the crossing of the threshold (our case). Besides that, they used χ_{DS} parameter to quantify the cluster dynamical state, which is very similar to our λ_{DS} as shown in Fig. 2. Therefore, we expect a similar scale between their merger time and our relaxation time. It is worth noting that their studies focus on major merger events ($\Delta_M/M \geq 0.5$), while we will provide a more statistical view of the relaxation period.

As shown in Fig. 5, one cluster can have more than one relaxation period during its evolution process. The distributions for relaxation periods for clusters in samples are shown in Fig. 6. The relaxation period is quantified as the median number of relaxation periods, which are 1.9 (1.8) Gyr, 1.6 (1.6) Gyr, and 1.4 (1.6) Gyr for DMO run, GX run, and GIZMO run, respectively, the numbers inside brackets are standard deviations.

4.3.1 Connection to the halo mass changes

The relaxation period provides valuable information about the evolution of cluster dynamical states, especially when connecting with the merger events. As mentioned above, it is intuitively correlated to the mass accretion history of a cluster, with an increase in halo mass leading to a decrease on λ_{DS}. It worth noting that there can be multiple $\frac{\Delta M_{200}}{M_{200}}$ peaks in a relaxation period, which corresponds to multiple mergers in the cluster formation.

To quantify such correlation, we start from simple cases which only contain one $\frac{\Delta M_{200}}{M_{200}}$ peak in a relaxation period. We leave the relaxation period with multiple peaks for validating our analytical

Table 1. The median numbers of the differences of (from left to right) η, Δ_r, f_s, and λ_{DS} between GX run (the first row)/GZIMO run (the second row) with standard errors and DMO run, The third row displays the median numbers of each parameter in DMO run.

	η	Δ_r	f_s	λ_{DS}
GX - DMO	-0.039 ± 0.232	-0.005 ± 0.030	-0.003 ± 0.036	0.289 ± 2.471
GIZMO - DMO	-0.034 ± 0.256	-0.003 ± 0.036	0.025 ± 0.036	0.180 ± 2.554
DMO	1.155	0.066	0.143	3.017

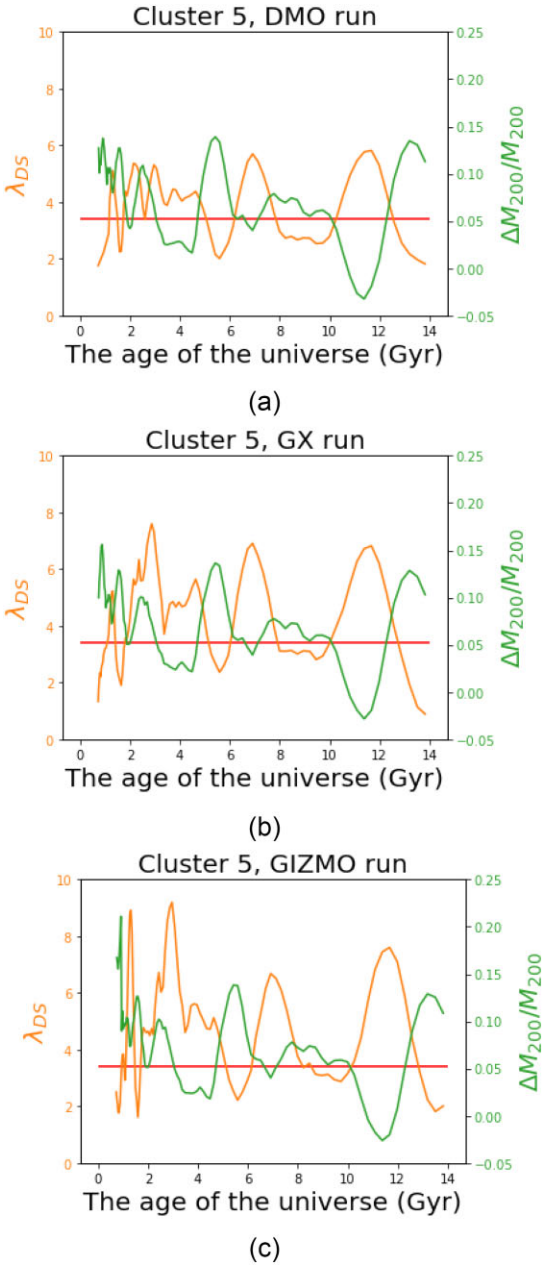

Figure 4. Evolution tracks of λ_{DS} (orange) and $\frac{\Delta M_{200}}{M_{200}}$ (green) over time for the fifth cluster, in (a) DMO run, (b) GX run, and (c) GIZMO run. The red horizontal line represents the threshold $\lambda_{DS} = 3.424$. The region above this line represents the cluster in a dynamically relaxed state.

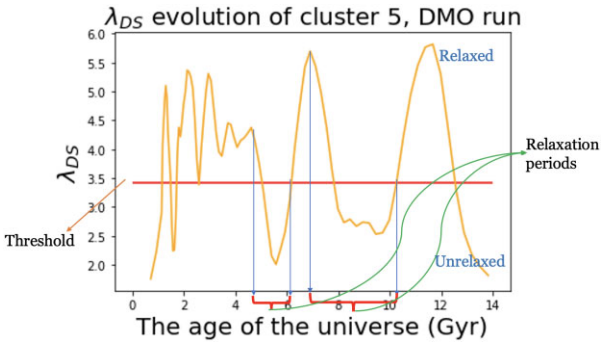

Figure 5. λ_{DS} evolutionary track for the fifth cluster in DMO run. The red brackets labels two relaxation periods identified in the evolutionary process of the cluster. The red horizontal line represents the threshold of cluster dynamical states, above and below which are relaxed and unrelaxed states, respectively.

formulae. Contradicting to our expectation, we do not find any strong correlation between the relaxation time period versus the maxima of fractional halo mass change. We think different mass accretions could cause this, for example, multiple small merge at the same time, or mass accretion from local environments versus a single major merger. Furthermore, the host halo mass may play an important role. For example, 10 per cent of mass accreting to a 10^{10} $M_\odot$ halo should have different relaxation periods compared to a 10^{15} $M_\odot$ halo. Therefore, we normalize the relaxation period with the dynamical time-scale, t_{dyn}, which is defined as

$$t_{dyn} = \left(\frac{R_{vir}^3}{GM_{vir}}\right)^{1/2}, \tag{9}$$

where R_{vir} and M_{vir} are virial radius and virial mass, respectively. Here, we simply adopt R_{200} as the virial radius and M_{200} as the virial mass. Then, we correlate the normalized relaxation period with the $\frac{\Delta M_{200}}{M_{200}}$ peak.

From equation (9), it is easy to show that the dynamical time-scale, t_{dyn}, is only a function of critical density, ρ_c, which solely depends on redshift z. Hence, the dynamical time-scale can be determined only with a given redshift. In this study, t_{dyn} is determined from the redshifts at which the relaxation periods start.

The scatter plots of relaxation period/dynamical time-scale versus $\frac{\Delta M_{200}}{M_{200}}$ are shown in Fig. 7. The Spearman rank-order correlation coefficient is 0.59/0.55/0.52 for DMO/GX/GIZMO run, which indicates a moderate correlation. Including more halo properties may give a better correlation. We retain that for a future study. Note that, as have discussed in Section 4.3, it is no surprise to see a similar distribution of t_{relax}/t_{dyn} in Fig. 7 compared to the fig. 3 of Contreras-Santos et al. (2022).

Then, we fitted these scatter plots with a linear function:

$$\frac{t_{relax}}{t_{dyn}} = k \times \frac{\Delta M_{200}}{M_{200}} + h \tag{10}$$

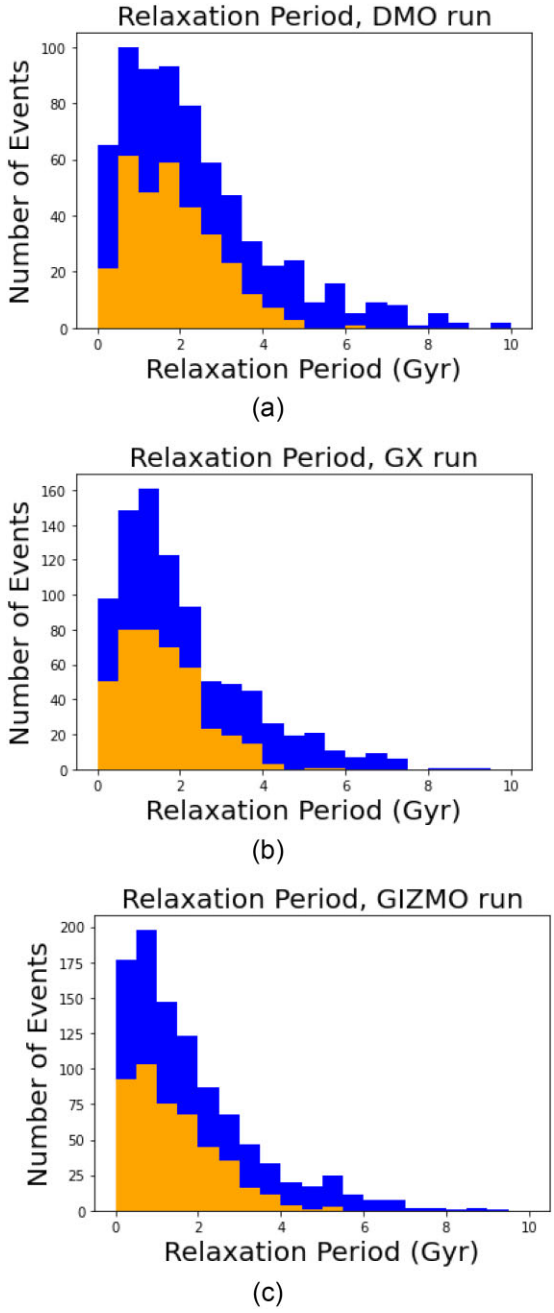

Figure 6. Relaxation period distribution for all clusters, in (a) DMO run, (b) GX run, and (c) GIZMO run. Blue bins represent all relaxation periods, orange bins represent relaxation periods with only one $\frac{\Delta M_{200}}{M_{200}}$ peak inside.

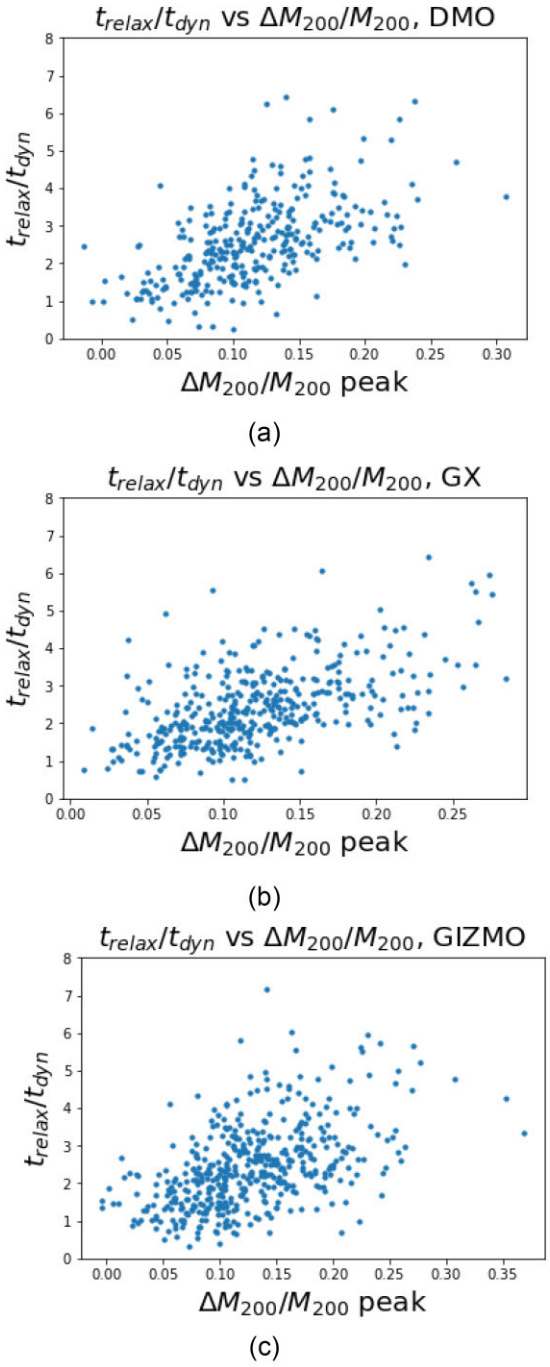

Figure 7. $\frac{t_{relax}}{t_{dyn}}$ versus $\frac{\Delta M_{200}}{M_{200}}$, for relaxation periods with single $\frac{\Delta M_{200}}{M_{200}}$ peak, for (a) DMO run, (b) GX run, and (c) GIZMO run.

and we obtain $k = 12.047/10.706/9.794$ and $h = 1.169/1.111/1.183$ from DMO/GX/GIZMO run, respectively. For the two hydrodynamical simulations, we calculate their mean square fitting errors and compare them with the mean square errors from DMO fitting function, i.e. data are from the hydrodynamical run. Still, predictions are made with equation (10) with parameters k and h yielded from DMO fitting. For GX run, the mean square error from DMO fitting ($k = 12.047$, $h = 1.169$) is 0.36, and that from GX fitting ($k = 10.706$, $h = 1.111$) is 0.34. For GIZMO run, the mean square error from DMO fitting is 0.34, and that from GIZMO fitting ($k = 9.794$, $h = 1.183$) is 0.33. The differences in mean square fitting errors from DMO fitting and hydrodynamical fitting are small in both cases. Therefore, we use the values of k and h from the DMO fitting for all three simulations.

The distributions of fitting errors for relaxation periods with single $\frac{\Delta M_{200}}{M_{200}}$ peak inside are shown in Fig. 8. Most errors between predicted and real relaxation periods (89 per cent/91 per cent/89 per cent for DMO/GX/GIZMO run) are less than ∼0.5 Gyr. These are considerably less than the median length of those relaxation periods with single $\frac{\Delta M_{200}}{M_{200}}$ peak, which is 1.847/1.577/1.413 Giga years in DMO/GX/GIZMO run. The median fitting errors of three distributions are close to 0, and slightly deviating towards a positive direction. The skewness and kurtosis of the distribution in DMO/GX/GIZMO

run are −1.159/−1.030/−0.461 and 3.075/4.050/2.429, respectively. The negative skewness means that there is more weight in the left tail of the distribution.

Given the linear correlation shown in Fig. 7, it is not surprising to see such a relatively small fitting error. To verify this fitting function, we adopt it for making predictions of the relaxation periods with more than one $\frac{\Delta M_{200}}{M_{200}}$ peaks by simply linear summation of contributions from all $\frac{\Delta M_{200}}{M_{200}}$ peaks:

$$t_{relax} = t_{dyn} \times \sum_{i=1}^{n} \left(12.047 \times \frac{\Delta M_{200,i}}{M_{200,i}} + 1.169 \right), \quad (11)$$

where t_{dyn} is calculated by the redshift at which the relaxation period starts, and n represents the total number of $\frac{\Delta M_{200}}{M_{200}}$ peaks that happen within the relaxation period. Note that a different t_{dyn} for each peak may give a better prediction. The distributions of fitting errors for those relaxation periods with multiple peaks inside are showed in Fig. 9. Most errors (82 per cent/88 per cent/88 per cent in DMO/GX/GIZMO run) are less than ∼2 Gyrs. However, the median numbers of these distributions deviate towards the positive direction ($\lesssim$ 0.5 Gyr), which means that equation (11) slightly overestimates the length of the relaxation period. The skewness and kurtosis for the distribution in DMO/GX/GIZMO run are 0.429/−0.008/0.042 and 3.602/2.363/3.371, respectively.

The fractional fitting error distributions of relaxation periods with multiple $\frac{\Delta M_{200}}{M_{200}}$ peaks for DMO, GX, and GIZMO run are plotted altogether in Fig. 10. The histograms are not normalized. The total number of relaxation periods identified in two hydrodynamical runs is significantly larger than that in DMO run, which implies an increased merger events by the baryon effect. 81.3 per cent/74.1 per cent/71.2 per cent of fractional errors in DMO/GX/GIZMO run are less than 0.6. The skewness and kurtosis for the distribution in DMO/GX/GIZMO run are 1.602/1.230/1.980 and 4.396/2.033/6.342, respectively. In agreement with the behaviours in absolute error distributions, all fractional error distributions deviate towards positive direction. The deviation of the median number of fractional fitting error is most substantial in the GIZMO run. The median number in GX run also has a larger deviation than that in DMO run.

5 CONCLUSIONS AND DISCUSSIONS

In this work, we use the mass-complete cluster sample from THE THREE HUNDRED to study the cluster dynamical states and proposed a new parameter λ_{DS} to classify the clusters into dynamical relaxed and unrelaxed without a manually set threshold. Benefiting from the different runs (DMO, GX, and GIZMO) within this project, we can also investigate the baryon effect on the cluster dynamical state. Furthermore, we define a relaxation period and connect it to the halo mass changes. The main findings are summarized below:

(i) Based on the relaxation parameter χ_{DS} in Haggar et al. (2020), a new threshold-free function of λ_{DS} is proposed to classify cluster dynamical states, which is

$$\lambda_{DS} = \sqrt{\frac{3}{(7.30 \times \Delta_r)^2 + (0.30 \times f_s)^2 + |1 - \eta|^2}} \quad (12)$$

The threshold distinguishing relaxed and unrelaxed states is naturally set by the double-Gaussian fitting of the λ_{DS} distribution. At redshift z = 0, 151/171/170 clusters of all 324 clusters are classified to be dynamically relaxed in DMO/GX/GIZMO run. The λ_{DS} parameter is linearly correlated to χ_{DS} parameter, and it preserves the classification results based on χ_{DS}.

(ii) Including baryons in simulations can slightly reduce the virial ratio η, which is 2 per cent lower in GX and GIZMO run compared to DMO run.

The baryonic effect results in the scattering distribution of the centre of mass offset, Δ_r, the standard deviation of the difference between Δ_r from GX/GIZMO run and DMO run is large (more than 50 per cent) compared to the scale of Δ_r from DMO run.

Subhalo mass fraction f_s is 17 per cent higher in the GIZMO run than in the DMO run, while the GX run is about 2 per cent lower.

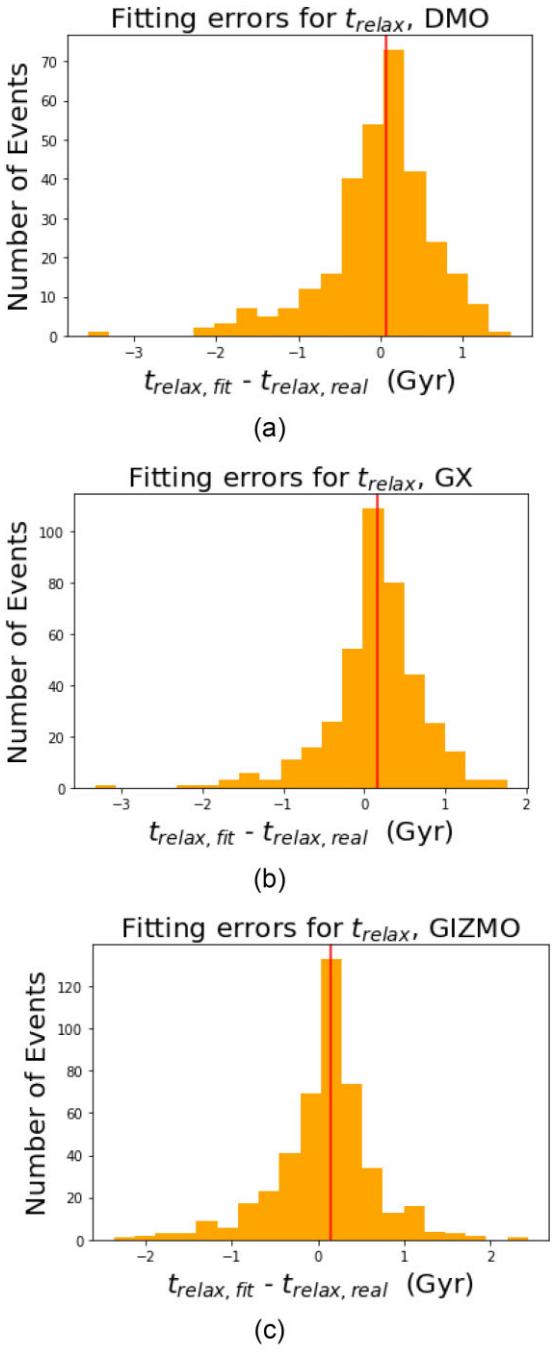

Figure 8. Fitting errors of relaxation periods with single $\frac{\Delta M_{200}}{M_{200}}$ peak inside the duration, for (a) DMO run, (b) GX run, and (c) GIZMO run. Red vertical line represents the median number of fitting errors.

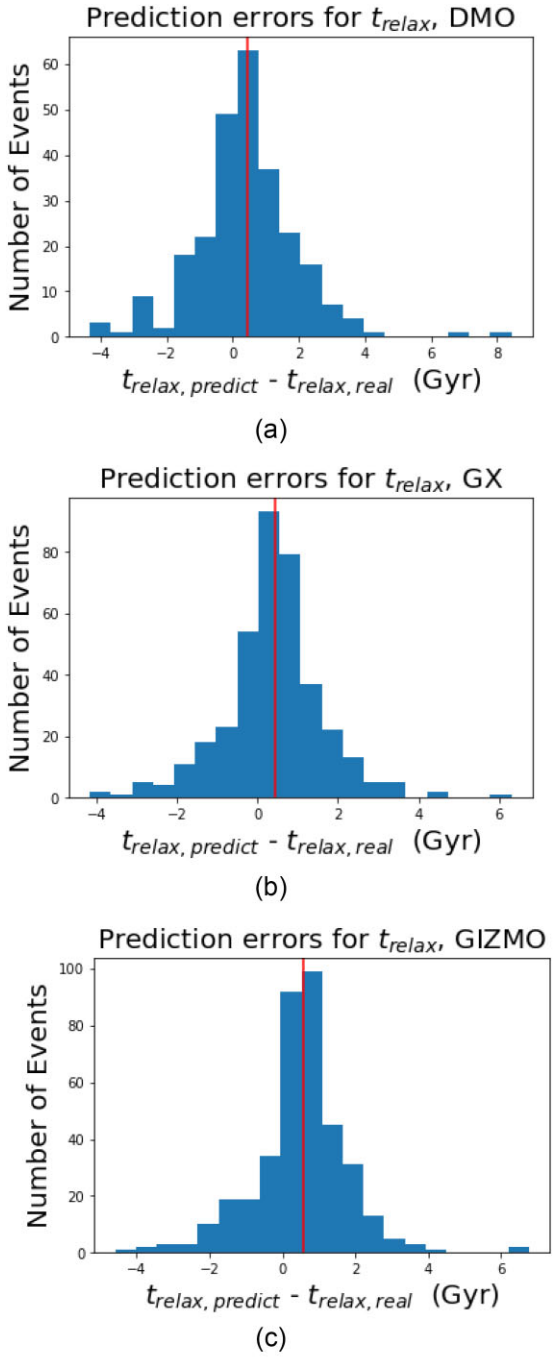

Figure 9. Prediction errors of relaxation periods with multiple $\frac{\Delta M_{200}}{M_{200}}$ peaks inside the duration, for (a) DMO run, (b) GX run, and (c) GIZMO run. Red vertical lines represent the median prediction errors.

In combination, the λ_{DS} in the GIZMO run is 3 per cent lower than in the GX run, which has about 10 per cent higher value than the DMO run. Therefore, more relaxed clusters are presented in the hydrodynamic simulations. Nevertheless, the baryons play a weak role in altering the cluster dynamical state.

(iii) The median number of relaxation periods (the time taken by a cluster to evolve from the most relaxed state to unrelaxed state and then return to relaxed state), also regarded as a relaxation period, is 1.913/1.610/1.419 for DMO/GX/GIZMO run, respectively.

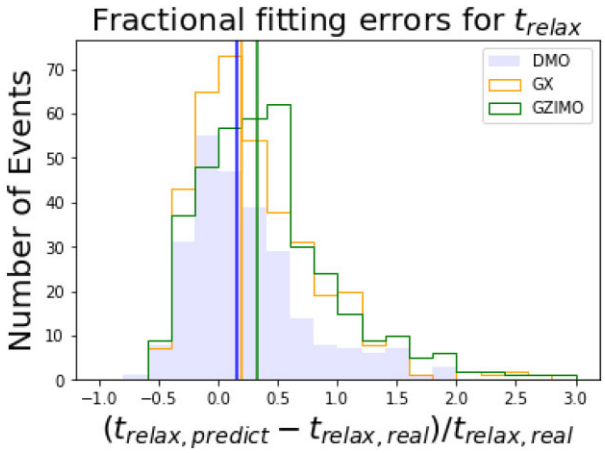

Figure 10. Distributions of the relative prediction errors, $(t_{relax,\,predict}$-$t_{relax,\,real})/t_{relax,\,real}$, for clusters in DMO (filled blue bins), GX (unfilled orange line), and GIZMO (unfilled green line) run. Blue/orange/green vertical line represents the median number of prediction error from DMO/GX/GIZMO run.

(iv) The relaxation period is correlated to cluster mass accretion history. For relaxation periods with a single $\frac{\Delta M_{200}}{M_{200}}$ peak inside, a moderate linear correlation is observed, which is described as

$$\frac{t_{relax}}{t_{dyn}} = 12.047 \times \frac{\Delta M_{200}}{M_{200}} + 1.169. \tag{13}$$

In general case, the length of relaxation periods can be predicted from the heights of $\frac{\Delta M_{200}}{M_{200}}$ peaks with

$$t_{relax} = t_{dyn} \times \sum_{i=1}^{n} \left(12.047 \times \frac{\Delta M_{200,i}}{M_{200,i}} + 1.169\right) \tag{14}$$

with a considerable small error, basically less than 2 Gyrs.

As shown in Fig. 2, the new proposed λ_{DS} is basically linear correlated with the χ_{DS}. So it can be correlated with these observational measured quantities, such as M (Cialone et al. 2018; De Luca et al. 2021) and $\mathcal{C}$ (Capalbo et al. 2021) parameters. The clusters can be naturally separated into relaxed and unrelaxed by applying its threshold from a double-Gaussian fitting,. With this single and non-arbitrary classification, it is straightforward to define some time-scale to describe the transition rate of dynamical states of a cluster. Such time-scale can be determined entirely from the features of the evolution track of λ_{DS} (see Fig. 5), which makes it applicable to be analysed statistically for a large number of clusters, thus evaluate its overall correlation with other observables (e.g. fractional mass change of cluster).

In this work, we only impose two constraints on the λ_{DS} parameter: having well-behaved Double-Gaussian distribution over clusters and preserving classification results with χ_{DS}. Meanwhile, the observed linear correlation between subhalo mass fraction f_s and centre of mass offset Δ_r is likely to introduce additional degrees of freedom in Double-Gaussian fitting. Therefore, we acknowledge that there may be some other values of a and b in equation (7), or even a different form of function to combine dynamical parameters together, which can make λ_{DS} satisfy our requirements. In future work, it will be worthy of investigating the potential improvement of the formalism of λ_{DS} with some advanced statistical methods.

Although the baryons can affect the cluster properties in different aspects (see Cui et al. 2016, for example), the cluster dynamical state seems to be less influenced by the baryons. That is understandable

as baryons have the strongest effect at very small scale, while the dynamical state describes the full dynamical information of the cluster. This is similar to baryon effects on the total cluster mass (see Cui et al. 2012; Cui, Borgani & Murante 2014, for example). Agreed with Zhang, Yu & Lu (2016), the baryon effect does shirk the cluster's relaxation period, which results in slightly more relaxed clusters in the hydrodynamical runs. However, unlike their ideal case study, which does not include any baryon processes in two-haloes merger event, the hydrosimulated clusters from THE THREE HUNDRED project do not show significantly change in the relaxation period. This can be explained as the merger speed and gas content are relatively low in reality, which is in agreement with their results – ∼70 per cent reduction in the merger time-scale.

Note that our definition of the cluster relaxation period is slightly different from the merger time, which is widely used in the semi-analytical models (for example Boylan-Kolchin, Ma & Quataert 2008; Jiang et al. 2008; Jiang & van den Bosch 2014). Our definition focused on the overall cluster dynamical state, while the merger time is mainly interested in the dynamical friction, for example, a satellite galaxy moving in a dark matter halo. The two time-scales are very similar when a major merger happens. Moreover, by using the relation between the cluster dynamical state relaxation period with the cluster mass changes in this study, one can roughly predict how long the cluster will return to a relaxed state.

As the merger events can lead to the cluster/galaxy property changes, Contreras-Santos et al. (2022) using the cluster dynamical changes (similar to our relaxation period definition) to define pre- and post-merger phases, we found that stellar content of BCGs grows significantly during mergers: The main growth mechanism is the accretion of older stars; there is a burst in star formation induced by the merger. Furthermore, the evolution of the hydrodynamic equilibrium bias can be also tightly connected to the major mergers (Gianfagna et al., in preparation). Therefore, through the observed accretion in mass, we can predict the cluster relaxation period, which can be used to predict the changes in these quantities.

ACKNOWLEDGEMENTS

We kindly thank Alexander Knebe, Ana Contreras, Elena Rasia, Frazer Pearce, and Roan Haggar for useful discussions.

This work has received financial support from the European Union's Horizon 2020 Research and Innovation programme under the Marie Sklodowskaw-Curie grant agreement number 734374, i.e. the LACEGAL project.

The simulations used in this paper have been performed in the MareNostrum Supercomputer at the Barcelona Supercomputing Center, thanks to CPU time granted by the Red Española de Supercomputación. The CosmoSim data base used in this paper is a service by the Leibniz-Institute for Astrophysics Potsdam (AIP). The MultiDark data base was developed in cooperation with the Spanish MultiDark Consolider Project CSD2009-00064.

WC is supported by the STFC AGP consolidated Grant ST/V000594/1 and the Atracción de Talento Contract no. 2020-T1/TIC-19882 granted by the Comunidad de Madrid in Spain. He further acknowledges the science research grants from the China Manned Space Project with no. CMS-CSST-2021-A01 and CMS-CSST-2021-B01. MDP acknowledges support from Sapienza Università di Roma thanks to Progetti di Ricerca Medi 2020, RM120172B32D5BE2.

DATA AVAILABILITY

The data used in this paper is provided by THE THREE HUNDRED project. It is available upon request.

REFERENCES

Acebron A. et al., 2019, ApJ, 874, 132
Anbajagane D. et al., 2022a, MNRAS, 510, 2980
Anbajagane D. et al., 2022b, MNRAS, 514, 1645
Ansarifard S. et al., 2020, A&A, 634, A113
Arthur J. et al., 2019, MNRAS, 484, 3968
Baldi R. D., Chiaberge M., Capetti A., Rodriguez-Zaurin J., Deustua S., Sparks W. B., 2013, ApJ, 762, 30
Baxter E. J., Adhikari S., Vega-Ferrero J., Cui W., Chang C., Jain B., Knebe A., 2021, MNRAS, 508, 1777
Beck A. M. et al., 2016, MNRAS, 455, 2110
Bett P., Eke V., Frenk C. S., Jenkins A., Helly J., Navarro J., 2007, MNRAS, 376, 215
Biffi V. et al., 2016, ApJ, 827, 112
Binney J., Tremaine S., 1987, Galactic dynamics. Princeton University Press, Princeton, N.J.
Boylan-Kolchin M., Ma C.-P., Quataert E., 2008, MNRAS, 383, 93
Capalbo V., De Petris M., De Luca F., Cui W., Yepes G., Knebe A., Rasia E., 2021, MNRAS, 503, 6155
Cialone G., De Petris M., Sembolini F., Yepes G., Baldi A. S., Rasia E., 2018, MNRAS, 477, 139
Contreras-Santos A. et al., 2022, MNRAS, 511, 2897
Cui W., Borgani S., Dolag K., Murante G., Tornatore L., 2012, MNRAS, 423, 2279
Cui W., Borgani S., Murante G., 2014, MNRAS, 441, 1769
Cui W. et al., 2016, MNRAS, 458, 4052
Cui W., Power C., Borgani S., Knebe A., Lewis G. F., Murante G., Poole G. B., 2017, MNRAS, 464, 2502
Cui W. et al., 2018, MNRAS, 480, 2898
Cui W., Davé R., Peacock J. A., Anglés-Alcázar D., Yang X., 2021, Nature Astron., 5, 1069
Cui W. et al., 2022, MNRAS, 514, 977
Davé R., Anglés-Alcázar D., Narayanan D., Li Q., Rafieferantsoa M. H., Appleby S., 2019, MNRAS, 486, 2827
Davis A. J., D'Aloisio A., Natarajan P., 2011, MNRAS, 416, 242
de Carvalho R. R., Ribeiro A. L. B., Stalder D. H., Rosa R. R., Costa A. P., Moura T. C., 2017, AJ, 154, 96
De Luca F., De Petris M., Yepes G., Cui W., Knebe A., Rasia E., 2021, MNRAS, 504, 5383
Díaz-García L. A., Umetsu K., Rasia E., Cui W., Meneghetti M., 2022, MNRAS, 512, 1214
Elahi P. J. et al., 2016, MNRAS, 458, 1096
Faltenbacher A., Diemand J., 2006, MNRAS, 369, 1698
Gianfagna G. et al., 2021, MNRAS, 502, 5115
Gouin C., Bonnaire T., Aghanim N., 2021, A&A, 651, A56
Haggar R., Gray M. E., Pearce F. R., Knebe A., Cui W., Mostoghiu R., Yepes G., 2020, MNRAS, 492, 6074
Haggar R., Pearce F. R., Gray M. E., Knebe A., Yepes G., 2021, MNRAS, 502, 1191
Hopkins P. F., 2015, MNRAS, 450, 53
Hou A., Parker L. C., Harris W. E., Wilman D. J., 2009, ApJ, 702, 1199
Jiang F., van den Bosch F. C., 2014, MNRAS, 440, 193
Jiang C. Y., Jing Y. P., Faltenbacher A., Lin W. P., Li C., 2008, ApJ, 675, 1095
Kim S. Y., Peter A. H. G., Wittman D., 2017, MNRAS, 469, 1414
Klypin A., Yepes G., Gottlöber S., Prada F., Heß S., 2016, MNRAS, 457, 4340
Knebe A. et al., 2020, MNRAS, 495, 3002
Knollmann S. R., Knebe A., 2009, ApJS, 182, 608
Kotecha S. et al., 2022, MNRAS, 512, 926
Kuchner U. et al., 2020, MNRAS, 494, 5473
Kuchner U. et al., 2021, MNRAS, 503, 2065
Li Q. et al., 2020, MNRAS, 495, 2930

Li Q., Han J., Wang W., Cui W., Li Z., Yang X., 2021, MNRAS, 505, 3907
Lopes P. A. A., Trevisan M., Laganá T. F., Durret F., Ribeiro A. L. B., Rembold S. B., 2018, MNRAS, 478, 5473
Mantz A. B., Allen S. W., Morris R. G., Schmidt R. W., von der Linden A., Urban O., 2015, MNRAS, 449, 199
McPartland C., Ebeling H., Roediger E., Blumenthal K., 2015, MNRAS, 455, 2994
Morell D. F., Ribeiro A. L. B., de Carvalho R. R., Rembold S. B., Lopes P. A. A., Costa A. P., 2020, MNRAS, 494, 3317
Mostoghiu R., Knebe A., Cui W., Pearce F. R., Yepes G., Power C., Dave R., Arth A., 2019, MNRAS, 483, 3390
Mostoghiu R. et al., 2021a, MNRAS, 501, 5029
Mostoghiu R. et al., 2021b, A&A, 652, A10
Nelson K., Rudd D. H., Shaw L., Nagai D., 2012, ApJ, 751, 121
Neto A. F. et al., 2007, MNRAS, 381, 1450
Pasquali A., Smith R., Gallazzi A., De Lucia G., Zibetti S., Hirschmann M., Yi S. K., 2019, MNRAS, 484, 1702
Poole G. B., Fardal M. A., Babul A., McCarthy I. G., Quinn T., Wadsley J., 2006a, MNRAS, 373, 881
Poole G. B., Fardal M. A., Babul A., McCarthy I. G., Quinn T. R., Wadsley J., 2006b, MNRAS, 373, 881
Rasia E. et al., 2015, ApJ, 813, L17
Roberts I. D., Parker L. C., 2017, MNRAS, 467, 3268
Rost A. et al., 2021, MNRAS, 502, 714
Sampaio V. M., de Carvalho R. R., Ferreras I., Laganá T. F., Ribeiro A. L. B., Rembold S. B., 2021, MNRAS, 503, 3065
Sayers J., Sereno M., Ettori S., Rasia E., Cui W., Golwala S., Umetsu K., Yepes G., 2021, MNRAS, 505, 4338
Sembolini F., Yepes G., De Petris M., Gottlöber S., Lamagna L., Comis B., 2013, MNRAS, 429, 323
Sembolini F. et al., 2016a, MNRAS, 457, 4063
Sembolini F. et al., 2016b, MNRAS, 459, 2973
Sereno M., Umetsu K., Ettori S., Sayers J., Chiu I. N., Meneghetti M., Vega-Ferrero J., Zitrin A., 2018, ApJ, 860, L4
Sereno M., Lovisari L., Cui W., Schellenberger G., 2021, MNRAS, 507, 5214
Shapiro S. S., Wilk M. B., 1965, Biometrika, 52, 591
Shaw L. D., Weller J., Ostriker J. P., Bode P., 2006, ApJ, 646, 815
Springel V., 2005, MNRAS, 364, 1105
Steinborn L. K., Dolag K., Hirschmann M., Prieto M. A., Remus R.-S., 2015, MNRAS, 448, 1504
Tamosiunas A., Briddon C., Burrage C., Cui W., Moss A., 2022, JCAP, 2022, 047
Thompson R., Davé R., Nagamine K., 2015, MNRAS, 452, 3030
Vega-Ferrero J., Dana J. M., Diego J. M., Yepes G., Cui W., Meneghetti M., 2021, MNRAS, 500, 247
Wang Y. et al., 2018, ApJ, 868, 130
Wen Z. L., Han J. L., 2013, MNRAS, 436, 275
Wong A. W. C., Taylor J. E., 2012, ApJ, 757, 102
Zenteno A. et al., 2020, MNRAS, 495, 705
Zhang C., Yu Q., Lu Y., 2016, ApJ, 820, 85

APPENDIX A: THE λ_{DS} DISTRIBUTIONS FOR GX AND GIZMO

It is interesting to see whether the parameters determined by the DMO run give similar distributions of λ_{DS} from the two hydroruns. Note that due to the baryon effect on the three key quantities: η, Δ_r, and f_s, the λ_{DS} distributions are not guaranteed to be double Gaussian. We show the results in Fig. A1. Although the distribution of λ_{DS} from GX can be fitted to double-Gaussian, there is a shift of the threshold value compared to the DMO result. While GIZMO can not be fitted by a double Gaussian distribution. Note that we never expect the hydrodynamic simulated clusters can be fitted by double Gaussian curve as the baryon models will change cluster dynamical state. Indeed, by looking at the baryon effects on individual key quantity in Fig. 4, we find that there is a shift in f_s for GIZMO compared to GX. Though the median λ_{DS} from GIZMO shows little change to the one from DMO, its distribution seems not to be fitted by a double-Gaussian curve. Nevertheless, we only interest in separating relaxed and un-relaxed clusters. Given its λ_{DS} values, as well as the fixed threshold from the DMO run, the relaxed and un-relaxed clusters from GIZMO are also fixed.

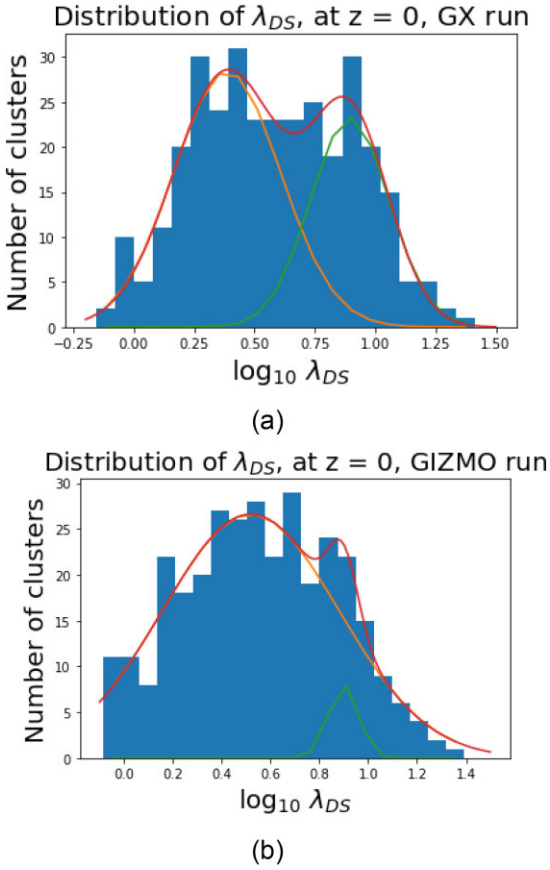

Figure A1. Distributions of relaxation parameter, λ_{DS}, in log10 scale (the same as Fig. 1) for 324 clusters at redshift $z = 0$, in GX run (a) and GIZMO run (b). Red lines represent Double-Gaussian fit and single-Gaussian fits are represented by orange and green lines in each plot.

APPENDIX B: λ_{DS} AND THRESHOLD FOR R500 DATA

For R500 data, a halo mass cut, $M_{500} = 4.6e14$ is applied to exclude low-mass clusters. Then the same method is applied to the left 246 clusters, and the free coefficients for λ in equation 7 are determined to be a = 15.85 and b = 1.04. The distribution of λ_{DS} for R500 is showed in Fig. B1.

The threshold is $\lambda_{DS} = 2.61$, as the X coordinate of the crossing point of two Single-Gaussian functions. With this threshold, 101 in 246 clusters are classified as relaxed.

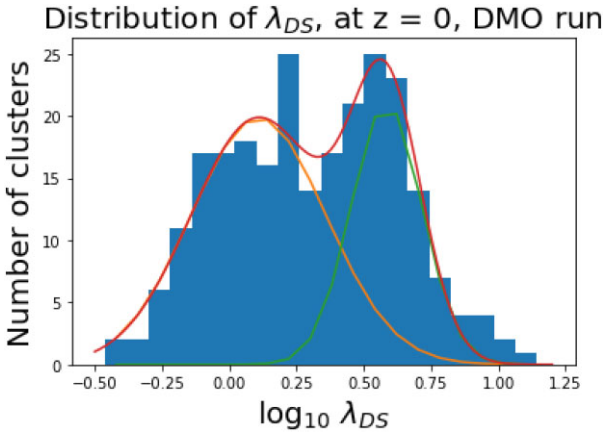

Figure B1. Distributions of the relaxation parameter, $\log_{10}\lambda_{DS}$, for the mass-complete cluster sample from the DMO run, R500, at redshift z $= 0$. The best-fitting parameters are $a = 15.85$ and $b = 1.04$. Red line represents the fitted Double-Gaussian distribution. The two single-Gaussian functions are represented by orange and green line.

This paper has been typeset from a TEX/LATEX file prepared by the author.